ELOVL4-Mediated Production of Very Long-Chain Ceramides Stabilizes Tight Junctions and Prevents Diabetes-Induced Retinal Vascular Permeability

Nermin M. Kady,[1] Xuwen Liu,[2] Todd A. Lydic,[1] Meesum H. Syed,[1] Svetlana Navitskaya,[1] Qi Wang,[1] Sandra S. Hammer,[1] Sandra O'Reilly,[1] Chao Huang,[1] Sergey S. Seregin,[3] Andrea Amalfitano,[3] Vince A. Chiodo,[4] Sanford L. Boye,[4] William W. Hauswirth,[4] David A. Antonetti,[2] and Julia V. Busik[1]

Diabetes 2018;67:769–781 | https://doi.org/10.2337/db17-1034

Tight junctions (TJs) involve close apposition of transmembrane proteins between cells. Although TJ proteins have been studied in detail, the role of lipids is largely unknown. We addressed the role of very long-chain (VLC ≥26) ceramides in TJs using diabetes-induced loss of the blood-retinal barrier as a model. VLC fatty acids that incorporate into VLC ceramides are produced by elongase elongation of very long-chain fatty acids protein 4 (ELOVL4). ELOVL4 is significantly reduced in the diabetic retina. Overexpression of ELOVL4 significantly decreased basal permeability, inhibited vascular endothelial growth factor (VEGF)– and interleukin-1β–induced permeability, and prevented VEGF-induced decrease in occludin expression and border staining of TJ proteins ZO-1 and claudin-5. Intravitreal delivery of AAV2-hELOVL4 reduced diabetes-induced increase in vascular permeability. Ultrastructure and lipidomic analysis revealed that ω-linked acyl-VLC ceramides colocalize with TJ complexes. Overall, normalization of retinal ELOVL4 expression could prevent blood-retinal barrier dysregulation in diabetic retinopathy through an increase in VLC ceramides and stabilization of TJs.

Loss of the blood-retinal barrier (BRB) and tight junction (TJ) integrity leads to increased permeability that marks early stages of diabetic retinopathy (DR). Several factors have been shown to contribute to increased vascular permeability, including diabetes-induced increase in the level of vascular endothelial growth factor (VEGF) (1–3), interleukin-1β (IL-1β) (4,5), tumor necrosis factor-α (TNF-α) (5), extracellular proteases, matrix metalloproteases 2 and 9 (6,7), and pericyte loss (8,9). Hyperglycemia is well known to induce proinflammatory and proangiogenic changes (10–12). However, the etiology of DR progression remains incompletely understood, and a recent assessment of the Diabetes Complications and Control Trial suggests that only 11% of blindness may be accounted for by hyperglycemia (13).

Recent clinical trials, including the Action to Control Cardiovascular Risk in Diabetes (ACCORD) Eye Trial, have demonstrated that in addition to hyperglycemia, dyslipidemia may contribute a critical role in the development of DR (14). Diabetic animal models have demonstrated that altered retinal lipid metabolism and dyslipidemia lead to retinal inflammation and vascular degeneration (15–17). Our laboratory identified a marked diabetes-induced decrease in the expression of several retinal fatty acid elongases. Elongation is a complex reaction that results in addition of two carbons to the carboxyl end of fatty acids. Seven elongation of very long-chain fatty acids (ELOVL1-7) have been identified in mammals, with each elongase exhibiting a characteristic substrate specificity and tissue distribution (18,19). Elongases are highly expressed in normal retina, where they actively participate in de novo lipogenesis as well as saturated, monounsaturated, and polyunsaturated fatty acid (PUFA) synthesis. Downregulation of elongases in the diabetic

[1]Department of Physiology, Michigan State University, East Lansing, MI
[2]Department of Ophthalmology and Visual Sciences, University of Michigan, Ann Arbor, MI
[3]Department of Microbiology & Molecular Genetics, Michigan State University, East Lansing, MI
[4]Ophthalmology and Molecular Genetics and Retina Gene Therapy Group, University of Florida, Gainesville, FL
Corresponding author: Julia V. Busik, busik@msu.edu.

Received 29 August 2017 and accepted 8 January 2018.
This article contains Supplementary Data online at http://diabetes.diabetesjournals.org/lookup/suppl/doi:10.2337/db17-1034/-/DC1.

retina results in an altered retinal fatty acid profile with decreased long-chain–to–short-chain fatty acids ratio (15).

ELOVL4, the highest expressed elongase in the retina (20), elongates extremely long fatty acids ≥C24 to produce ≥C26 very long-chain PUFA (VLCPUFA) and saturated VLC fatty acids (VLCFAs) (21–23). Saturated VLCFAs are primarily incorporated into ceramides and glucosylceramides (18,19). These ceramides with extremely long fatty acids are major lipid components of the stratum corneum and have been shown to be essential in maintenance of the water permeability barrier in skin (18,24,25). ELOVL4 is important for the maintenance of skin barrier function as ELOVL4$^{-/-}$ mice are neonatally lethal due to skin barrier defect (26–28). Besides the role of ELOVL4 in the skin, ELOVL4 dysfunction has been associated with Stargardt-like macular dystrophy (STGD3) (29,30). Interestingly, ELOLV4 is one of the enzymes that was found to be downregulated in the retina by both diabetes and retinal ischemia-reperfusion (31).

We hypothesized that VLC ceramides support BRB function in an ELOVL4-dependent manner. This study was designed to test the role of ELOVL4 and VLC ceramides in diabetes-induced increase in retinal vascular permeability and to identify whether lipids, in particular VLC ceramides, localize in the TJ and play a role in controlling the paracellular permeability of retinal endothelial cells.

RESEARCH DESIGN AND METHODS

Cell Culture

Bovine retinal endothelial cells (BREC, passage 4–6) were isolated and cultured as previously described (2). For biochemical purification of TJ, ARPE-19 cells were grown in DMEM/F12 (1:1 ratio, 5 mmol/L glucose) supplemented with 10% FCS and 1% penicillin/streptomycin at 37°C in humidified 95% air and 5% CO_2.

Virus-Mediated Human ELOVL4 Overexpression

Human ELOVL4 (hELOV4) was expressed using an E-1– and E-3–deleted adenoviral vector system containing the hELOVL4 cDNA (AdhELOVL4) under the control of the cytomegalovirus promoter. Subconfluent BRECs were transduced with AdhELOVL4 or AdEmpty as a negative control at a multiplicity of infection 20,000 overnight in Molecular, Cellular, and Developmental Biology (MCDB) media supplemented with 2% serum. Overexpression was confirmed by quantitative real-time PCR (qPCR) and immunoblotting for hELOVL4 at the time of permeability studies (60 h after viral transduction).

For in vivo experiments, hELOVL4 was engineered into adeno-associated virus serotype 2 vectors containing four capsid tyrosine to phenylalanine (Y–F) mutations (AAV2 mut quad) (32) under the control of the ubiquitous truncated chimeric cytomegalovirus-chicken β-actin (smCBA) promoter. Empty AAV2 mut quad construct was used as a negative control. The virus was produced at the Department of Ophthalmology, University of Florida, Gainesville, FL.

Small Interfering RNA Transfection

BREC were resuspended in Nucleofector solution (Amaxa Biosystems, Gaithersburg, MD) to a final concentration 5×10^5 cells/100 μL, mixed with 100 nmol/L control or ELOVL4 Stealth small interfering (siRNA) from Invitrogen Life Technologies (Carlsbad, CA), electroporated (Nucleofector program S-005; Amaxa Biosystems), and maintained in culture as above.

Permeability Assay In Vitro

Ad-Empty and Ad-hELOVL4 BRECs were grown on 0.4-μm pore Transwell filters (Corning Costar, Acton, MA) for 24 h and treated with hydrocortisone for 36 h and with recombinant human $VEGF_{165}$ (50 ng/mL for 30 min) or IL-1β (10 ng/mL for 15 min), where indicated, before the addition of rhodamine isothiocyanate (RITC)-dextran. BREC paracellular permeability to 70 kDa RITC-dextran (Sigma-Aldrich, St. Louis, MO) was measured for 4 h as previously described (2,3). The average permeability for control conditions (AdEmpty) used in all experiments ranged from 2.5 to 2.8×10^{-6} cm/s.

Western Blot

Protein extraction and Western blot was performed using NuPAGE system (Invitrogen) as previously described (3,17).

Real-time qPCR

Total RNA was extracted from BRECs or mouse retinas using Qiagen RNeasy (Qiagen, Valencia, CA) according to the manufacturer's instructions. Human and mouse gene-specific primers for ELOVL4 were used. Expression levels were normalized to bovine GAPDH or mouse cyclophilin.

Immunocytochemistry

Cellular localization of the TJ complexes in BRECs and mouse retina was evaluated by immunocytochemistry as described previously (5). TJ protein staining at the cell border was quantified by semiquantitative ranking score system as previously described (5). For colocalization, confocal images were analyzed using Nikon NIS Elements software to determine the Pearson coefficient of colocalization.

To evaluate TJ protein organization in retinal vasculature, whole-retina flat mounts were immunolabeled for occludin using mouse monoclonal anti-occludin Alexa Fluor 488 conjugate (1:75) (Cat. No. OC-3F10; Thermo Fisher Scientific). Images were acquired using a Nikon C2 microscope (Nikon Instruments, Melville, NY).

Immunogold Electron Microscopy

For conventional sample preparation (33), bovine retinas were fixed in 2.5% glutaraldehyde and 2.5% paraformaldehyde in 0.1 mol/L cacodylate buffer, postfixed in 2% osmium tetroxide in 0.1 mol/L cacodylate buffer, dehydrated in a graded series of acetone, and infiltrated and embedded with Spurr resin. Thin sections (60–70 nm) were obtained with a PowerTome ultramicrotome (RMC; Boeckeler Instruments, Tucson, AZ) and double-stained with uranyl acetate and lead citrate. Electron micrographs were obtained with a JEOL 100 CX (Japan Electron Optical Laboratory, Tokyo,

Japan) transmission electron microscope operated at 100 kV and equipped with a Gatan ORIUS CCD camera.

For double immunogold labeling (34), samples were fixed in 4% paraformaldehyde and 0.5 glutaraldehyde in PBS, dehydrated in a gradient series of ethanol, and infiltrated and embedded in LR White. Ultrathin sections were collected on a Formvar coated gold grid. Immunolabeling was performed by first placing the grid, section side down, in drops of 0.10 mol/L PBS (pH 7.4) containing 1% (weight for volume [w/v]) BSA. The grids were then transferred to a drop of the primary antibodies rabbit polyclonal anti-occludin (Cat. No. 71-1500; Invitrogen) and mouse monoclonal anti-ceramide (Cat. No. C8104; Sigma-Aldrich), diluted 1:1 in PBS-BSA for 2 h. The grids were rinsed in several changes of PBS and 0.5% (v/v) BSA and were floated on a 1:20 (v/v) dilution of goat anti-rabbit IgG conjugated with 15 nm gold and goat anti-mouse IgG conjugated with 6 nm gold in PBS-BSA. Finally, the grids were rinsed in PBS and distilled water. Negative control included the omission of the primary antibody. Grids were subsequently stained with 2% uranyl acetate and Reynold's lead citrate. Specimens were observed with a JEOL 100CX transmission electron microscope at an accelerating voltage of 100 kV.

TJ Isolation and Mass Spectrometry

TJs were isolated as previously described (35). Briefly, ARPE-19 cells (15- × 150-mm culture plates) were lysed with hypo-osmotic buffer, collected, homogenized, and centrifuged at 100,000*g* for 60 min at 4°C against a saturated sucrose cushion. The collected membrane was subsequently cryolysed using liquid nitrogen and then incubated with rabbit polyclonal anti–protein kinase C (PKC)-ζ (Cat. No. P 0713; Sigma-Aldrich) or rat monoclonal anti–ZO-1 (Cat. No. MABT11; Millipore) using protein A or G Dynabeads, respectively, according to the manufacturer's instructions (Invitrogen). TJ complexes bound to the beads were subjected to lipid extraction as previously described (36). Lipids obtained from TJs were analyzed by high-resolution/accurate mass spectrometry (MS) and tandem MS (MS/MS) in positive and negative ionization modes, using an LTQ-Orbitrap Velos MS (Thermo Fisher Scientific). Sphingolipids were identified as previously described in positive ion mode as $[M+H]^+$ and $[M-H_2O+H]^+$ molecular ions (37) and in negative ion mode as $[M+HCOO-H]^-$ ions (38). Ceramides of interest were further examined by higher-energy collisional dissociation MS/MS at 100,000 resolving power to confirm sphingolipid backbone and head group moieties. Mouse epidermal lipid extracts were used for optimization of analytical conditions for detecting putative VLCFA-containing sphingolipids.

Animal Model

All procedures involving animals were performed according to the Association for Research in Vision and Ophthalmology (ARVO) Statement for the Use of Animals in Ophthalmic and Vision Research and were approved and monitored by the Michigan State University Institutional Animal Care and Use Committee. Diabetes was induced in C57BL/6J male mice by streptozotocin (STZ), as previously described (39), and confirmed by blood glucose higher than 13.8 mmol/L (300 mg/dL). After 2 weeks of confirmed diabetes, animals received an intravitreal injection of AAV2-hELOVL4 quad mutant (right eye) or AAV2-Empty vector (left eye) as a control (2×10^9 viral genomes/eye in 1 μL). Average body weights and nonfasting blood glucose levels of control and diabetic mice are reported in Table 1. Animals were sacrificed 6–8 weeks after the viral injection (8–10 week of STZ induction) for retinal vascular permeability and retinal analysis.

Retinal Vascular Permeability

Mice were injected with fluorescein isothiocyanate-albumin (0.5 mg in 50 μL PBS) (Sigma-Aldrich). Blood was collected after 2 h, and the animal was perfused with 1% formaldehyde and enucleated. Retinas were removed and flat mounted. Images were acquired using a Nikon C2 scanning laser confocal microscope and measured using MetaMorph imaging software (Molecular Devices, Downingtown, PA) by subtracting residual fluorescence inside the vessels from total fluorescence to determine leakage fluorescence intensity. The fluorescence intensity of the leakage was averaged between at least five fields for each retina and normalized to the blood plasma fluorescence level (39).

Immunohistochemistry

Retinas were processed and immunolabeled as previously described (40). Colocalization of ELOVL4 with retinal vasculature was quantified using MetaMorph imaging software.

Statistical Analyses

Data are expressed as mean ± SEM. Results were analyzed for statistical significance by the Student *t* test or one-way ANOVA, followed by the post hoc Tukey test. GraphPad Prism 7 (GraphPad Software, San Diego, CA) was used for all statistical analysis. Significance was established at $P < 0.05$.

RESULTS

Expression Level of ELOVL4 Controls Retinal Endothelial Permeability

The effect of ELOVL4 on vascular permeability was evaluated in the monolayer of BRECs after overexpression or inhibition of ELOVL4. hELOVL4 was significantly expressed in adhELOVL4 transduced BRECs compared with AdEmpty transduced cells (Fig. 1*A* and *B*), with human-specific qPCR primers revealing expression only after transduction of the human exogenous gene (Fig. 1*A*), whereas Western blot revealed a 50% increase in steady state ELOVL4 over endogenous protein (Fig. 1*B*). Overexpression of hELOVL4

Table 1—Average body weights and nonfasting blood glucose level of control and diabetic mice

Group	*N*	Weight (g)	*P* value	Blood glucose (mg/dL)	*P* value
Control	17	29.6 ± 0.95	<0.0001	181.6 ± 4.62	<0.0001
Diabetic	25	24.6 ± 0.33		479.4 ± 21.26	

resulted in a significant decrease in permeability to 70 kDa RITC-dextran (53.7 ± 5.7% of control (Fig. 1*C*).

ELOVL4 mRNA and protein levels were significantly reduced in BRECs transfected with ELOVL4 siRNA compared with control siRNA (Fig. 1*D* and *E*). Knockdown of ELOVL4 was associated with increased paracellular permeability (528.2 ± 242.2% of control) (Fig. 1*F*).

ELOVL4 Overexpression Prevents VEGF- and IL-1β–Induced Increase in Permeability

Monolayers of AdhELOVL4 and AdEmpty transduced BRECs were treated with VEGF (50 ng/mL, 30 min) or IL-1β (10 ng/mL, 15 min). Paracellular permeability to 70 kDa RITC-dextran was measured. VEGF (Fig. 1*G*) and IL-1β (Fig. 1*H*) significantly increased cell permeability. hELOVL4 overexpression prevented VEGF- and IL-1β–induced increase in permeability (Fig. 1*G* and *H*, respectively).

ELOVL4 Overexpression Increases the Barrier Properties of the TJ Complex

As shown in Fig. 2*A*, overexpression of hELOVL4 significantly increased occludin content in AdhELOVL4-tranduced BRECs compared with AdEmpty transduced cells and prevented the VEGF-induced decrease in occludin. No significant effects of hELOVL4 on total protein expression were observed for ZO-1 and claudin-5 (Fig. 2*B* and *C*); however, immunostaining revealed that overexpression of hELOVL4 increased protein staining at the cell border and also prevented VEGF-induced disruption of continuous immunostaining of ZO-1 and claudin-5 at the cell border (Fig. 2*D* and *E*).

Ceramide Colocalizes With TJ Complex

Ceramide (green) was found to colocalize with the TJ complexes and follow the same distribution as ZO-1 and claudin-5 at the cell border (Fig. 2*D* and *E*). Quantification of ceramide colocalization of with ZO-1 or claudin-5 in confocal images revealed an average Pearson coefficient of colocalization of 0.77 and 0.65, respectively. In addition to cell border distribution, typical punctate green cytoplasmic staining of ceramides was observed.

To further verify ceramide localization in TJs, we performed immunogold labeling and transmission electron microscopy using the retinal vasculature in bovine retinas. TJs were observed as electron-dense structures with characteristic "kissing junction" configuration in specimens postfixed by osmium tetroxide (Fig. 3*A*). Neighboring sections were used for immunogold labeling of occludin and ceramide. As shown in Fig. 3*B*, ceramide (smaller, 6-nm gold particles) is localized along the TJ in proximity with occludin protein (larger, 15-nm gold particles) as well as in the intercellular space between two neighboring endothelial cells (Fig. 3*B*, right, upper panel). To establish the immunolabeling specificity of the anti-ceramide antibody, negative controls were included with the omission of the primary antibody (Fig. 3*C*).

To further determine the specificity of the anti-ceramide antibody, ARPE 19 cells were treated with 15 μmol/L desipramine (acid sphingomyelinase inhibitor), 50 μmol/L fumonisin (ceramide synthase inhibitor), or both, and ceramide immunofluorescent staining was analyzed (Supplementary Fig. 1). Inhibition of acid sphingomyelinase or ceramide synthase significantly reduced ceramide immunostaining compared with control.

Identification of Putative VLC ω-Linked Acyl-Ceramide Species in the TJ Complex

Negative ion MS of plasma membrane and TJs isolated from ARPE-19 cells using cryolysis, followed by immunoprecipitation with anti–PKC-ζ antibody, is shown in Fig. 4*A* and *B*, respectively. In addition to typical abundant plasma membrane phospholipids and sphingolipids, the high mass regions of the spectra in Fig. 4 contain charge/mass ratio (m/z) values matching the theoretical masses and isotope distributions of acyl-ceramide (AcylCer) molecular species. The assignment of these ions was further supported by Orbitrap high-resolution/accurate mass higher-energy collisional dissociation MS/MS to evaluate the presence of the sphingosine backbone. These data combined with accurate mass-based formula prediction and available published data suggest an assignment of AcylCer d18:1/h24:0 with an ω–*O*-linked linoleic acid (26–28). Identical analysis was performed on mouse epidermal lipid extracts where VLC AcylCer are known to be present. Ceramide molecular species in TJs isolated by immunoprecipitation with anti–ZO-1 antibody were comparable to those obtained from anti–PKC-ζ immunoprecipitation, including the presence of the putative AcylCer(d18:1/h24:0) at m/z 986.8393, identified as AcylCer(h42:1) in negative-ion MS analysis. In addition, similarly putative ω-linked d18:1/28:6 at m/z 1014.8131 and d18:1/30:6 at m/z 1042.8444 were detected at lower abundance, identified as AcylCer(46:7) and AcylCer(48:7).

Positive ion mode Orbitrap higher energy collisional dissociation MS/MS data and further details of ion identification are presented in Supplementary Fig. 2.

Relative quantitation of all detected ceramide species in ARPE-19 plasma membranes and TJs is shown in Fig. 4*C*.

ELOVL4 Overexpression Increases VLCFA and Ceramide Production

Lipids were extracted from monolayers of AdhELOVL4 and AdEmpty transduced BRECs and analyzed by high-resolution/accurate MS and MS/MS. As expected, ELOVL4 overexpression resulted in an increase in saturated and unsaturated free VLCFAs (Fig. 5*A*). In addition, free fatty acid levels of palmitic (16:0) and stearic (18:0) acids were increased in AdhELOVL4 transduced BRECs (Fig. 5*A*). Interestingly, there was an increase in overall sphingolipid abundance in AdhELOVL4 versus AdEmpty transduced BRECs, with increases in sphingomyelin and ceramide levels (Fig. 5*B*). Among the ceramide species, there were significant increases in Cer(d18:1/16:0), as well as ceramides with 24 carbon saturated, monosaturated, and PUFAs and VLC (26*C*) ceramides (Fig. 5*C*).

Verification of AAV2-Mediated Expression of hELOVL4 in Mouse Retinas

In agreement with our previous study (15), ELOVL4 mRNA expression was reduced in diabetic retinas compared with

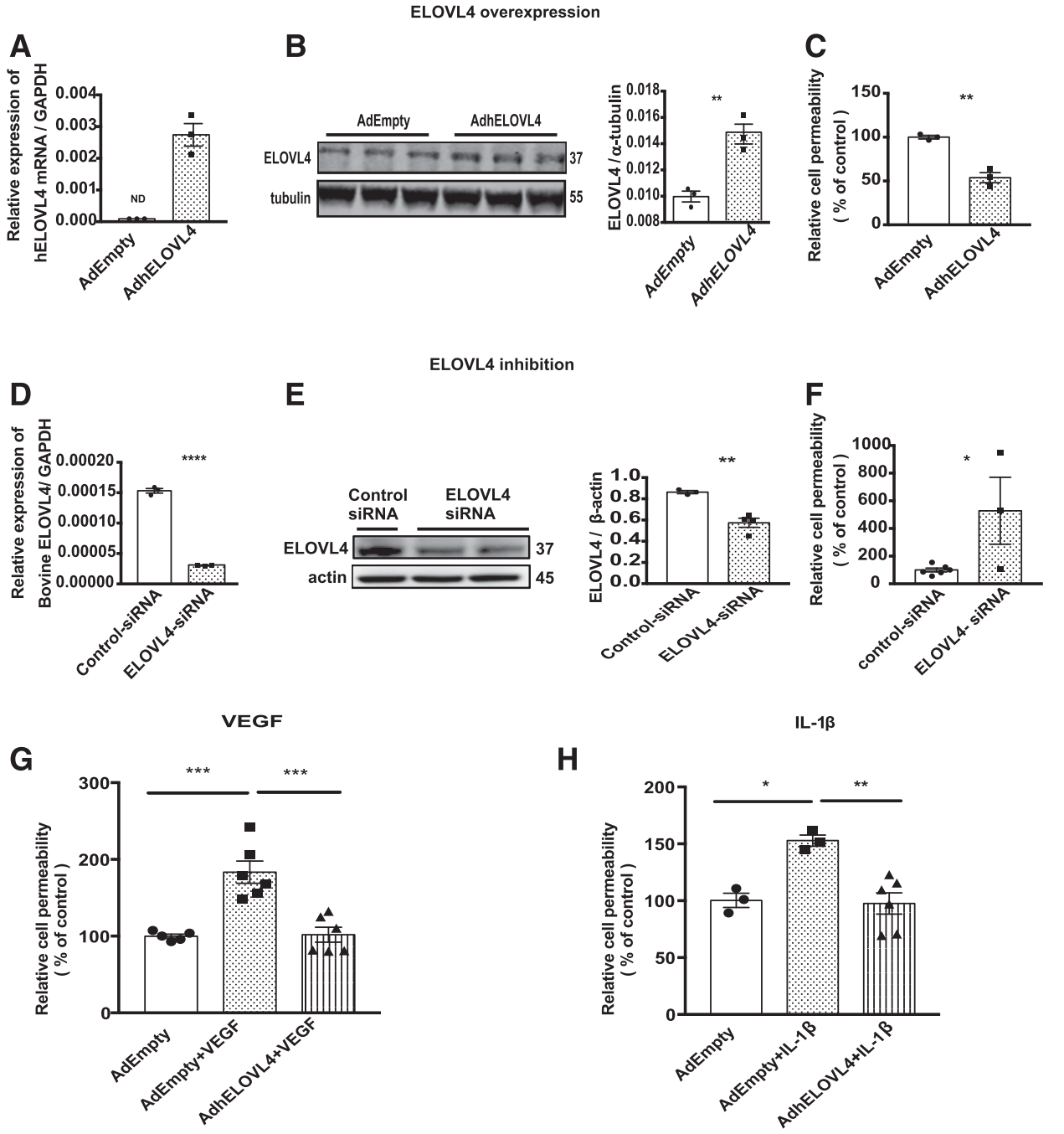

Figure 1—Expression level of ELOVL4 controls retinal endothelial permeability. BRECs were transduced with AdEmpty or AdhELOVL4 and collected 60 h after adenovirus transduction for RNA analysis by real-time qPCR (*A*) or protein by Western blot (*B*) to confirm adenovirus-mediated overexpression of hELOVL4. hELOVL4 mRNA expression was normalized to GAPDH (*A*), and protein expression was normalized to α-tubulin loading control (*B*). Data from three independent experiments, different cell isolates, triplicate wells each, are presented. *C*: Paracellular permeability to 70 kDa RITC-dextran was determined in BRECs transduced with AdEmpty or AdhELOVL4 in untreated cells. Data from triplicate wells, three measurements each, are presented. *A–C*: Circles, control; squares, ELOVL4. *D–F*: BRECs were transfected with control siRNA or ELOVL4-siRNA and collected for analysis. Three independent siRNA experiments, each in triplicate, were performed. Expression profile of ELOVL4 was determined by real-time qPCR, 48 h after transfection (*D*), or Western blot, 72 h after transfection (*E*), to confirm silencing of ELOVL4. Bovine ELOVL4 mRNA expression was normalized to GAPDH (*D*), and protein expression was normalized to β-actin loading control (*E*). *F*: Paracellular permeability to 70 kDa RITC-dextran was determined in BRECs transfected with control siRNA or ELOVL4 siRNA. *D–F*: Circles, control; squares, ELOVL4 siRNA. Paracellular permeability to 70 kDa RITC-dextran was determined in BRECs transduced with AdEmpty (circles), AdEmpty treated with VEGF (*G*) or IL-1β (*H*) (squares), or AdhELOVL4 treated with VEGF (50 ng/mL) for 30 min (*G*) or treated with IL-1β (10 ng/mL) for 15 min (*H*) (triangles). The VEGF experiment was repeated three times in two different laboratories by two investigators, six samples per condition, with seven time points per sample. The IL-1β with ELOVL4 overexpression experiment was performed with six samples per condition, seven time points per sample. Results are shown as mean ± SEM. ND, not determined; $^{*}P < 0.05$, $^{**}P < 0.01$, $^{***}P < 0.001$, $^{****}P < 0.0001$.

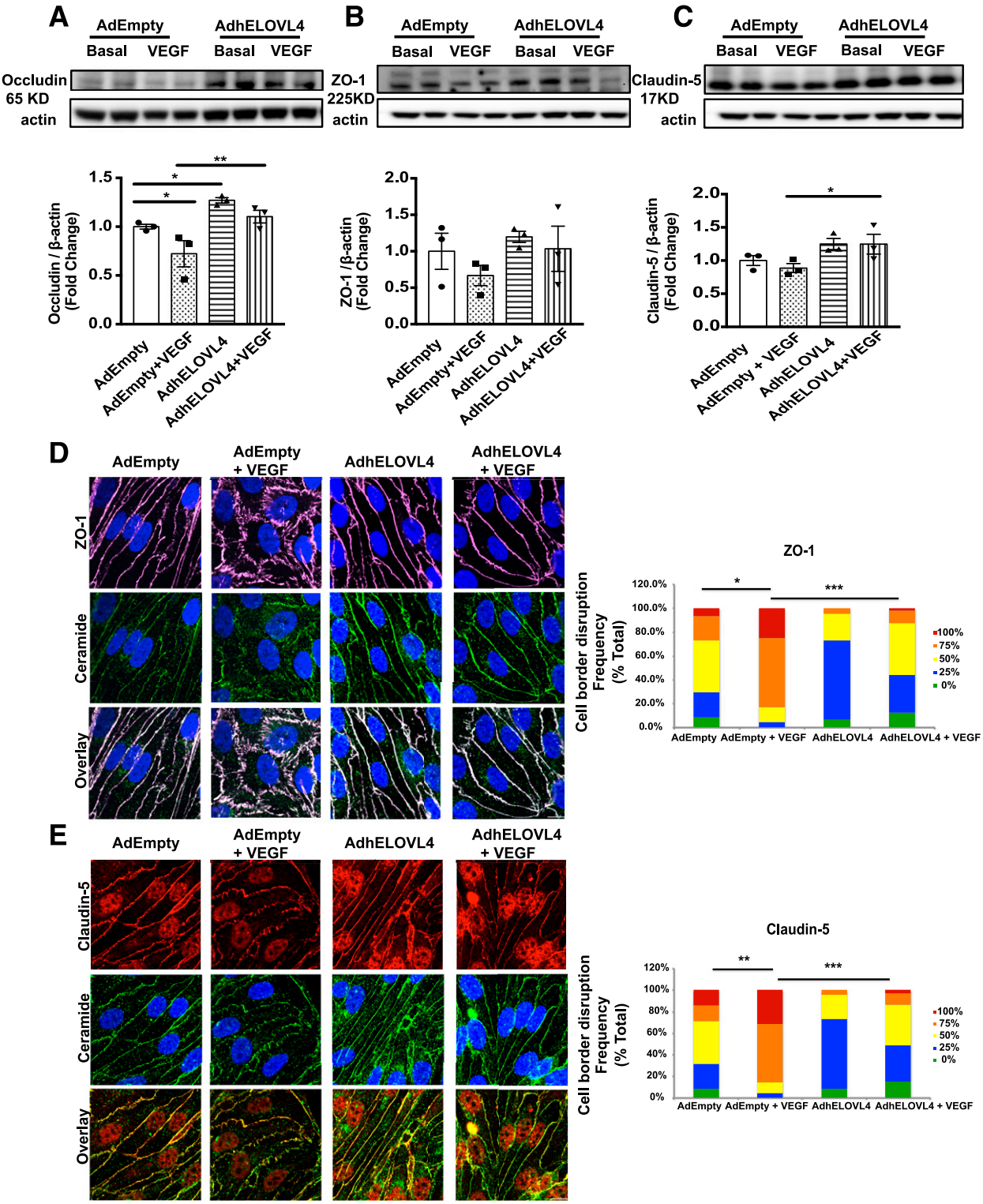

Figure 2—ELOVL4 overexpression increases the barrier properties of TJ complex. *A–C*: Confluent AdEmpty and AdhELOVL4 transduced BRECs were treated with VEGF (50 ng/mL) for 30 min. Total cell lysates were immunoblotted for occludin (*A*), ZO-1 (*B*), and claudin-5 (*C*). β-Actin served as the loading control. The experiment was repeated twice in triplicate. Representative Western blots from three independent experiments are shown on top, with densitometry quantification below. Results are shown as mean ± SEM. Circles, control; squares, control with VEGF; triangles, ELOVL4; upside-down triangles, VEGF with ELOVL4. *D* and *E*: Confluent monolayers of BRECs treated as in *A–C* were immunolabeled for ZO-1 (far red) and ceramide (green) (*D*) or claudin-5 (red) and ceramide (green) (*E*), and confocal images were taken. The results are from two independent experiments; for each condition, four images were examined. Four fields were analyzed for each image. Scale bars, 10 μm. Quantification of each protein staining at the cell border is shown on the far right. The results represent the frequency of each score as described in RESEARCH DESIGN AND METHODS. $^{*}P < 0.05$, $^{**}P < 0.01$, $^{***}P < 0.001$.

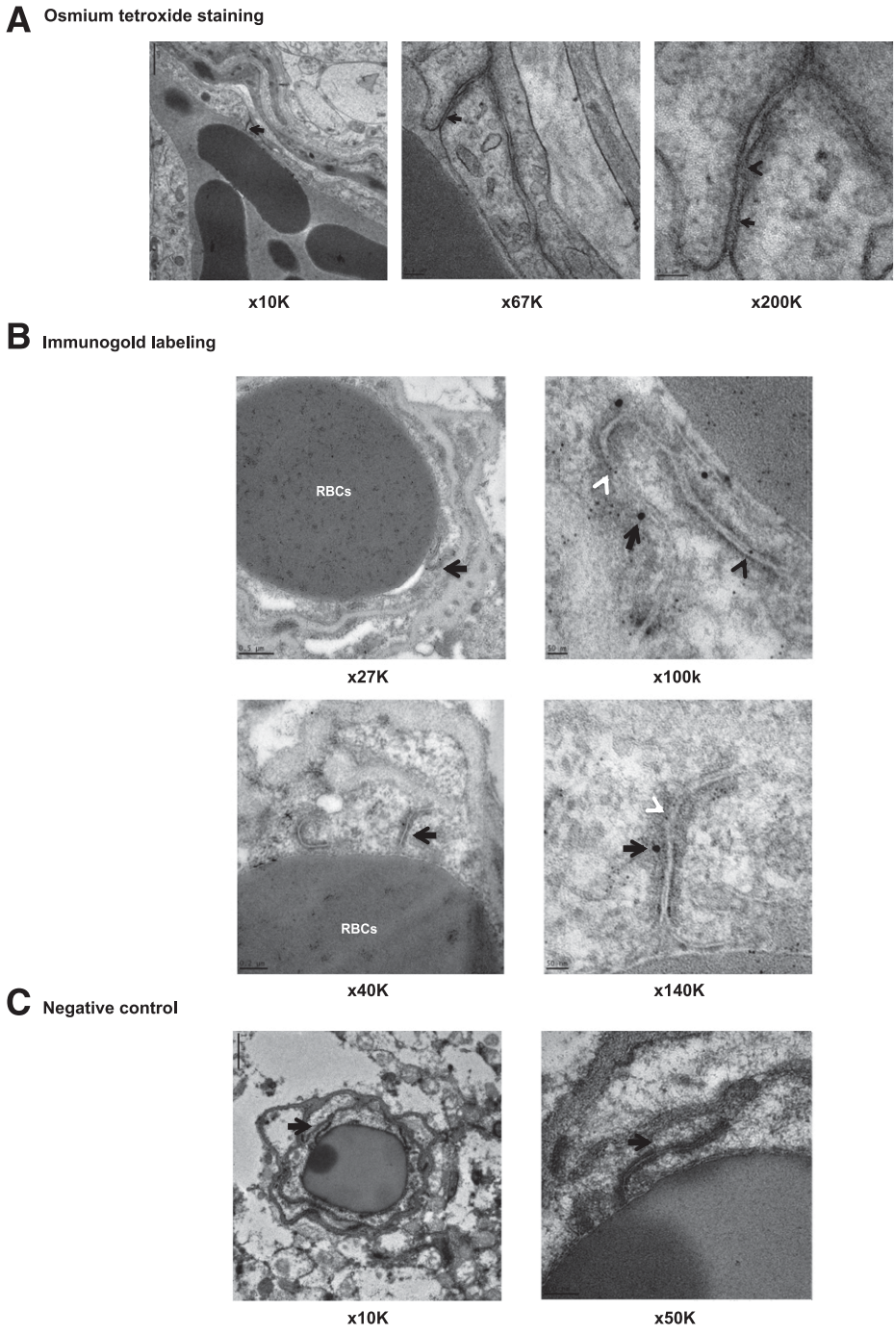

Figure 3—Ceramide colocalizes with TJ complex. *A*: TJs stained by osmium tetroxide (OsO_4) staining (black arrows). Lower original magnification ×10,000, red blood cells (RBCs) in the intravascular compartment and the TJ between two neighboring retinal endothelial cells (black arrow) (left). Scale bar, 1 μm. TJ is enlarged for better visualization original magnification ×67,000 (black arrow) (middle). Scale bar, 0.1 μm. Kissing point, hallmark of tight junction (black arrowhead) (right). Scale bar, 0.5 μm. *B*: Immunogold localization of ceramide and TJ protein occludin in ultrathin sections of bovine retina. *B* (left panel): Lower original magnification ×27,000 (upper) and ×40,000 (lower) of the tight junction (black arrow), with RBC in the intravascular compartment. Scale bars, 0.5 μm and 0.2 μm, respectively. *B* (right panel): Higher original magnification ×100,000 (upper) and ×140,000 (lower). Ceramide (smaller, 6-nm gold particles) (white arrowhead) localized along the TJ in juxtaposition to the TJ protein, occludin (larger, 15-nm gold particles) (black arrow). Scale bars, 50 nm. Although most of the ceramide labeling is localized along the cytoplasmic side of the plasma membrane, it can also be visualized in the intercellular space between two neighboring endothelial cells (black arrowhead). The TJs from 3 retinas were imaged; representative images from 26 independent images are shown. *C*: Negative controls are representative images of the TJs where primary antibodies were omitted. Lower original magnification ×10,000 of the tight junction (black arrow), with RBC in the intravascular compartment (left panel). Scale bar, 1 μm. Higher magnification of the tight junction ×50,000 (black arrow) (right panel). Scale bar, 200 nm.

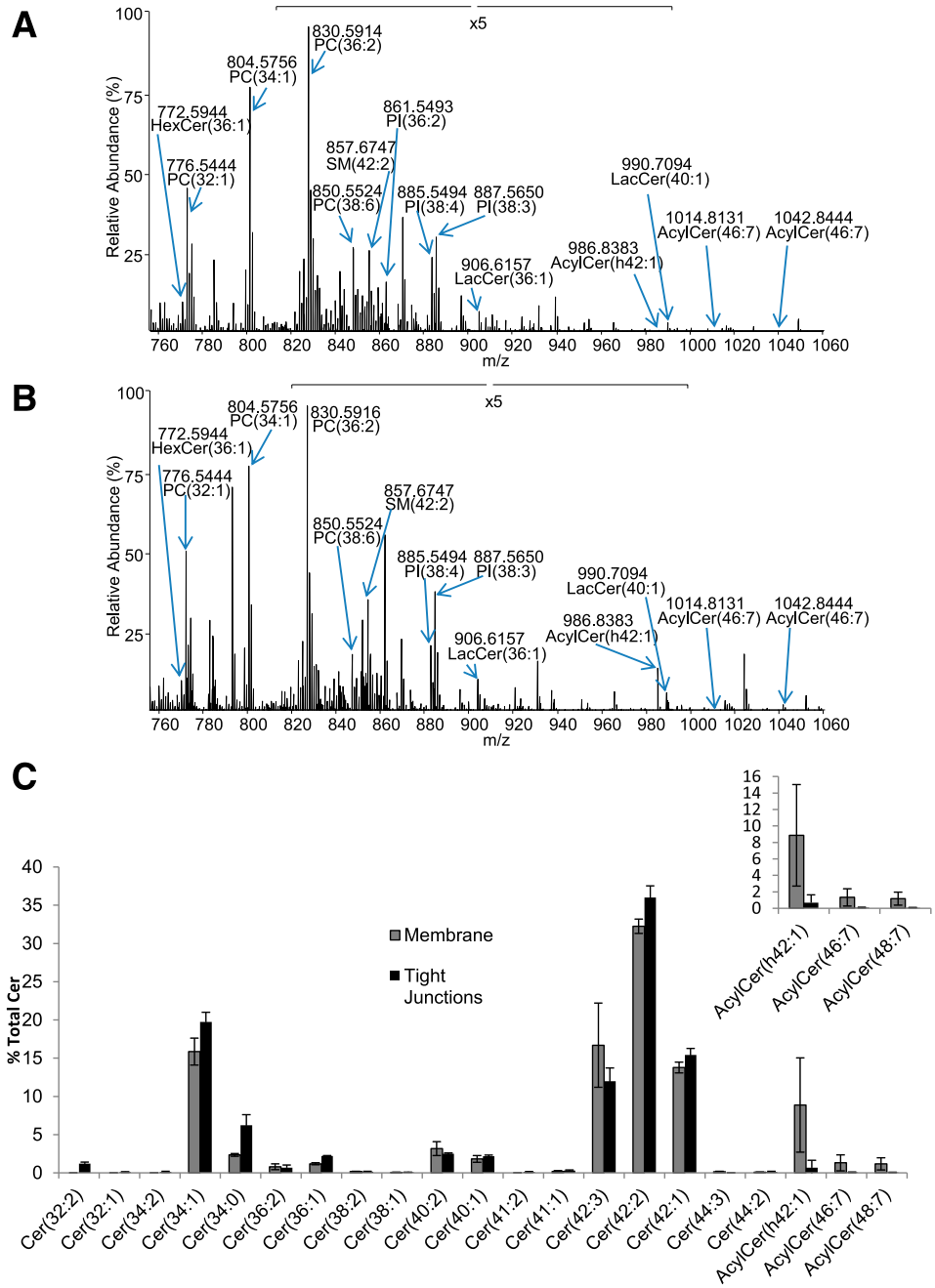

Figure 4—High resolution/accurate MS lipidomic analysis of ARPE-19 plasma membrane and TJ fractions. Negative ion Orbitrap high resolution/accurate MS of ARPE-19 plasma membrane (*A*) and ARPE-19 TJ lipid extracts (*B*) at 100,000 resolution. Sphingolipids and phosphatidylcholine lipids were detected as $[M+HCO_2-H]^-$ ions under the analytical conditions used. The indicated region was original magnified ×5 to enhance spectral detail. *C*: Quantitation of ceramide molecular species observed in ARPE-19 plasma membrane and TJ fractions. The inset indicates putative VLCFA-containing AcylCer species. HexCer, hexosylceramide; LacCer, lactosylceramide; PC, phosphatidylcholine; PI, phosphatidylinositol; SM, sphingomyelin.

control (Fig. 6*A*). Transduction with AAV2- hELOVL4 led to hELOVL4 overexpression in diabetic and nondiabetic retinas as determined using human transgene-specific primers. As expected, the hELOVL4 transcript was undetectable in AAV2-Empty injected in the contralateral retinas (Fig. 6*B*).

To determine the effect of diabetes with and without AAV2-hELOVL4 overexpression on vascular levels of ELOVL4, retinal cross sections were immunolabeled for ELOVL4 (green). Isolectin-B4 (red) was used to counterstain the retinal vasculature. AAV2-Empty injected retinas were used as the control. Diabetes induced downregulation of endothelial expression of ELOVL4, which was reversed by AAV2-hELOVL4 treatment (Fig. 6*C*).

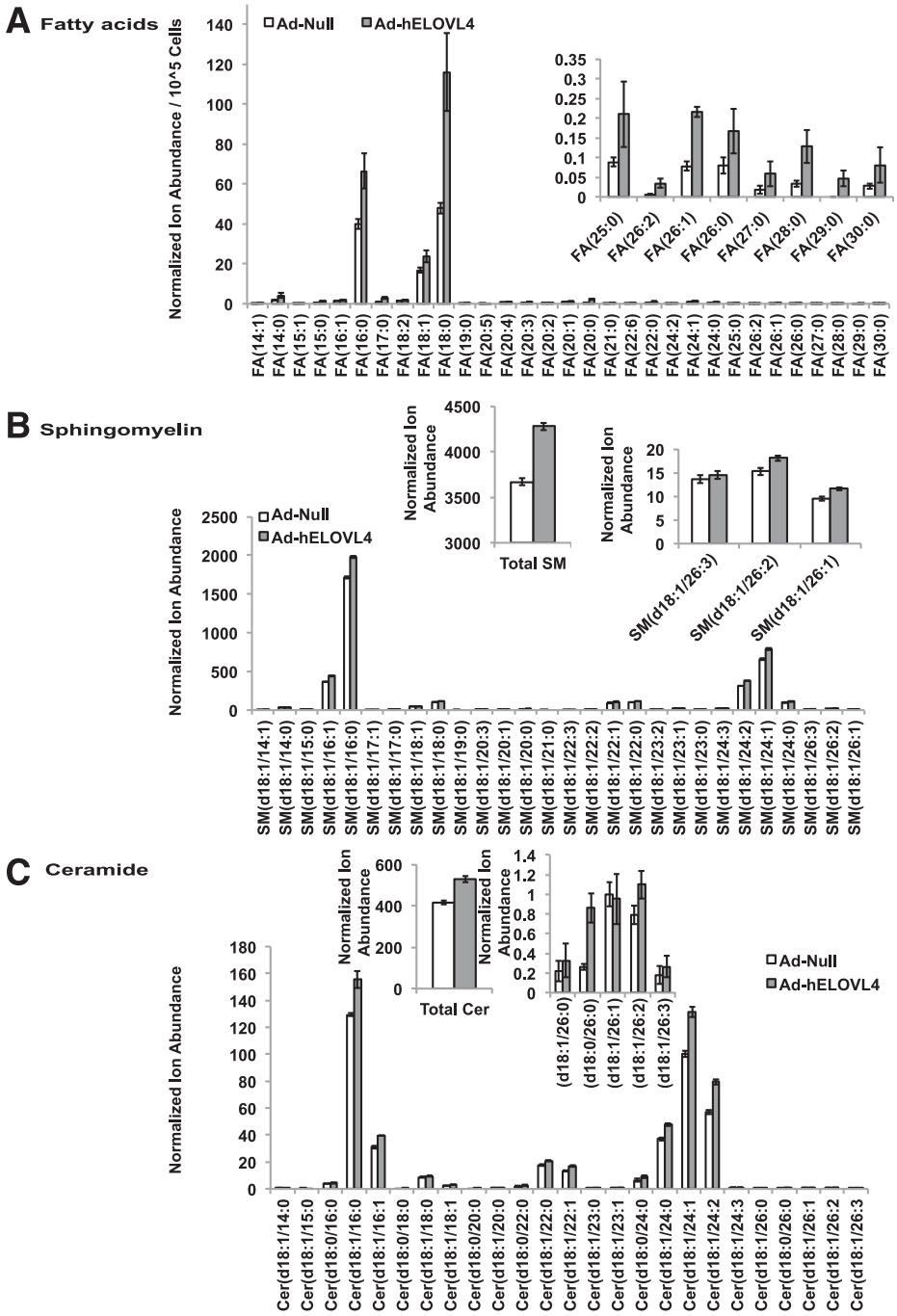

Figure 5—ELOVL4 overexpression increases free fatty acids (FA), sphingomyelin (SM), and ceramide levels in hELOVL4-transfected bovine retinal endothelial cells. *A*: Individual free fatty acids were measured by nESI-Orbitrap high resolution/accurate MS. Inset: Normalized ion abundance of fatty acids greater than C24. *B*: Total and individual sphingomyelin molecular species were measured by nESI-Orbitrap high resolution/accurate MS. Left inset: Total normalized ion abundance of all sphingomyelin species detected in control and hELOVL4-transfected cells. Right inset: Normalized abundance of SM species containing fatty acids greater than C24. *C*: Total and individual ceramide molecular species were measured by nESI-Orbitrap high resolution/accurate MS. Left inset: Total normalized ion abundance of all ceramide species detected in control and hELOVL4-transfected cells. Right inset: Normalized abundance of ceramide species containing fatty acids greater than C24. Results were obtained from three independent transfections. Results are shown as mean ± SD.

AAV2-hELOVL4 Overexpression Prevents Diabetes-Induced Increase in Retinal Vascular Permeability

Diabetes induced a significant increase in vascular permeability (5.6-fold of control) (Fig. 6*D*) in retinas receiving AAV2-Empty vector (left eye) relative to nondiabetic controls (left eye). Notably, treatment with AAV2-hELOVL4 (right eye) prevented the diabetes-induced increase in vascular permeability. Fluorescein isothiocyanate-albumin leakage

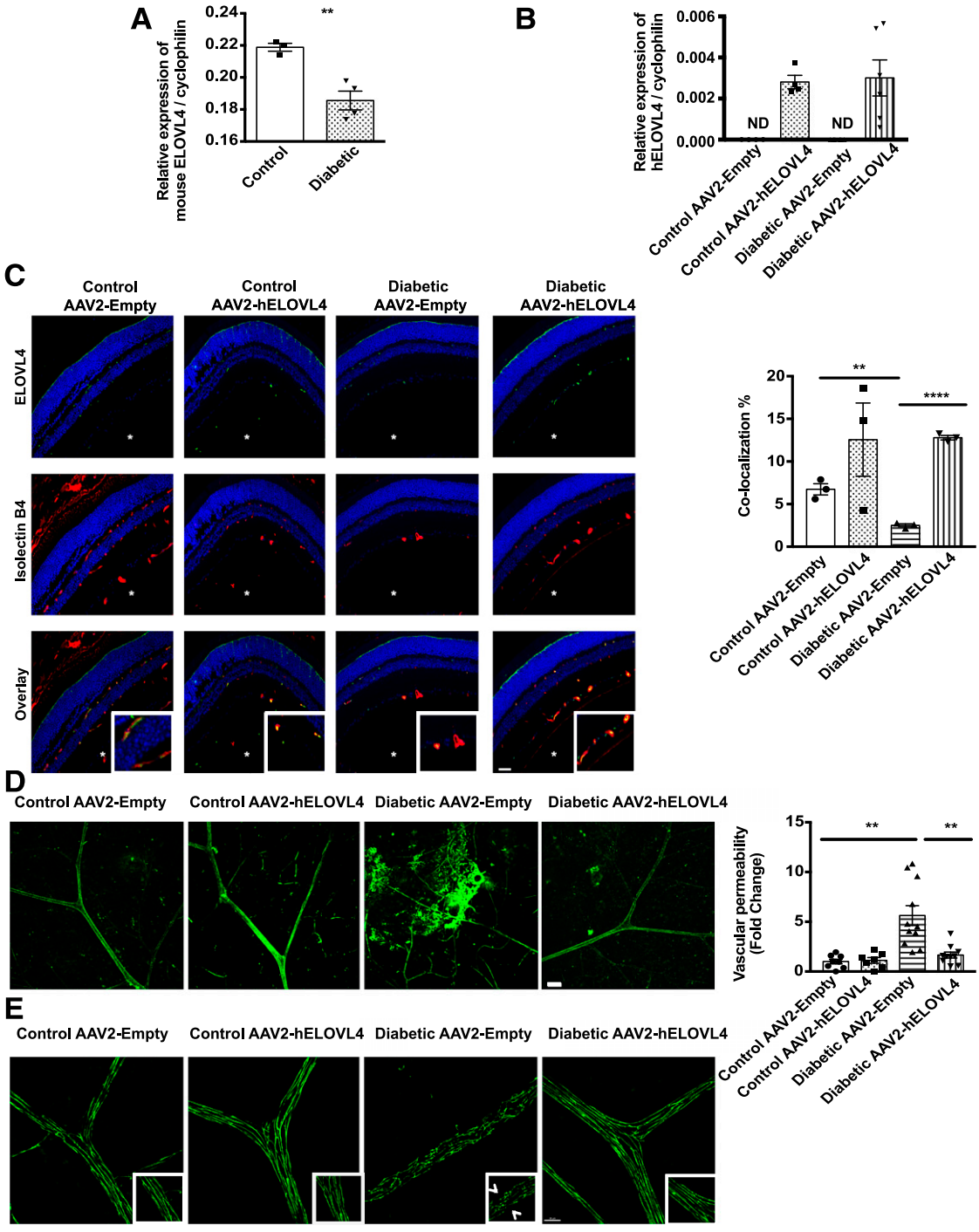

Figure 6—ELOVL4 overexpression prevents diabetes-induced vascular leakage in mice. STZ-induced diabetic mice were intravitreally injected with AAV2-hELOVL4 mut quad (right eye) or control AAV2-Empty vector (left eye) 2 weeks after diabetes induction. Retinal tissue was analyzed 6–8 weeks after the viral injection. *A*: Real-time qPCR quantification of endogenous mouse ELOVL4 mRNA levels in control (squares) and diabetic (triangles) retinas. The experiment was repeated four times by different investigators, with three to six animals per condition in each experiment. *B*: Real-time qPCR quantification of exogenous human ELOVL4 mRNA levels in control and diabetic retinas. Four control and six diabetic animals were used, and the experiment was performed in triplicate. *C*: Immunohistochemical detection of ELOVL4 (green, upper panel) colocalization with retinal vasculature (red, middle panel), with yellow color (lower panel) indicating vascular expression in retinal cross-sections. Quantification of colocalization (yellow) is shown on the far right. Circles, control; squares, control with ELOVL4; triangles, diabetic; upside-down triangles, diabetic with ELOVL4. Three retinas per condition were used, and images from three fields were taken. Scale bar, 20 μm. The vitreous side is indicated with a white asterisk. *D*: Representative fluorescent images of retinal vascular permeability. Retina permeability was evaluated by measuring leakage fluorescence intensity as shown on the far right (8 control and 12 diabetic animals used in the study). Scale bar, 50 μm. *E*: Immunostaining of flat-mounted whole retinas for occludin. Arrowheads show disruption of continuous staining in diabetic retinas. Representative images from three different retinas, and three to six images per retina are shown. Scale bar, 20 μm. ND, not determined. $^{**}P < 0.01$, $^{****}P < 0.0001$.

was significantly lower in diabetic mouse retinas receiving AAV2-hELOVL4 (right eye) than AAV2-Empty diabetic mouse retinas (left eye; 1.6-fold of control) (Fig. 6*D*).

To confirm the beneficial effect of ELOVL4 overexpression on TJ distribution at the cell border, whole-retina flat mounts were immunolabeled for occludin in AAV2-Empty and AAV2-hELOVL4 transduced retinas. In AAV2-Empty diabetic retinas (left eye), occludin immunoreactivity was evidently disrupted and intermittently lost in retinal blood vessels. These changes were prevented in AAV2-hELOVL4 diabetic retinas (right eye), where occludin distribution was similar to that of control mice (Fig. 6*E*).

DISCUSSION

Elongases and desaturases are key enzymes in fatty acid metabolism; they regulate the length and degree of saturation of fatty acids and thereby their function and metabolic fate. The expression level of elongases and desaturases in the liver and retina is affected by diabetes, with dramatic downregulation of elongases, including the most abundant retinal elongase, ELOVL4, in the retina (15,41–43). ELOVL4 has a substrate specificity profile for fatty acids of C24 or longer and can elongate polyunsaturated, monounsaturated, and saturated VLCFAs (22). The role of ELOVL4 in the retina was mainly described for VLCPUFA (44–46). VLCPUFAs are present in the rod outer-segment membrane, where they are suggested to contribute a role in photoreceptor function by stabilizing the rims of photoreceptor disks (44).

Although the highest retinal expression of ELOVL4 is found in the photoreceptor inner segment (30), it is also expressed in other retinal layers (47,48). Here, we demonstrated expression of ELOVL4 in the retinal vasculature. The product of ELOVL4-mediated elongation will depend on the precursor fatty acids. Because the photoreceptors are rich in n-3 PUFA, the main products of ELOVL4 in photoreceptor cells are C32-36 PUFAs. Endothelial and epithelial cells have lower n-3 PUFA and higher saturated fatty acids content leading to a higher level of saturated VLCFA production that can be incorporated into ceramides. This is further supported by the studies demonstrating that ELOVL4 works in concert with ceramide synthases leading to VLC ceramide production (49). Specifically, ceramide synthase 3 synthesizes ceramides with very long acyl chains (49). We demonstrated that ELOVL4 overexpression in BREC significantly increased VLC saturated, monosaturated, and PUFA production. The overall abundance of sphingolipids, both sphingomyelin and ceramide, was increased by ELOVL4 overexpression. Interestingly, in addition to VLC free fatty acids and ceramides, ELOVL4-overexpressing cells had higher palmitic and stearic free fatty acid levels and ceramides with 16- and 24-chain fatty acids. These data reflect the complex nature of the cross talk between lipid metabolic pathways. Overexpression of ELOVL4 in BREC could affect the rate of ceramide production through the ceramide synthase pathway. Because saturated fatty acids are an integral part of ceramide production, increased levels of palmitic and stearic acids could be a reflection of the overall activation of ceramide production in these cells.

The role of VLC ceramides is best known in the skin permeability barrier, where they represent a major component of the stratum corneum (26–28). Whether a decrease in ELOVL4 and thus VLC ceramides production in the retina plays a role in BRB breakdown in diabetes was not known and represented a major focus of this study.

Overexpression of ELOVL4 by recombinant adenoviral system normalized VEGF- and IL-1β–induced retinal vascular permeability in BRECs and increased steady state content of the TJ protein occludin. Further, cell border organization was normalized for ZO-1 and claudin-5. Importantly, intravitreal delivery of hELOVL4 in the diabetic retina using an AAV2 viral vector increased hELOVL4 expression in retinal endothelium and prevented the diabetes-induced increase in vascular permeability. These data strongly support the role of ELOVL4 in a protective probarrier function.

Although this is the first study to demonstrate the role of ELOVL4 in the retinal BRB, the essential role of ELOVL4 in skin barrier function is well known. Homozygous ELOVL4 mutant mice die within few hours after birth due to defective skin barrier and severe dehydration (26–28), a phenotype that can be rescued by skin-specific expression of ELOVL4 to normalize skin permeability (50). This defective water insulation function of the skin was attributed to ELOVL4 loss of function and the subsequent decrease in the production of VLCFA ($C \geq 26$) and thereby VLC ceramides and AcylCers, critical lipid components of the skin barrier function. The VLC ceramides, and especially ω-linked AcylCer species, have never been shown outside of the stratum corneum. Moreover, this is the first demonstration of these unusual lipids in the TJ structure. The plasma membrane preparation contains TJs; thus, the presence of AcylCers in the total plasma membrane is not surprising. Moreover, TJs were enriched in overall ceramides compared with total plasma membrane; thus, the decrease in the percentage of total of ω-*O*-AcylCer in tight junctions is the function of an overall increase in total ceramides rather than lower ω-*O*-AcylCer levels.

Ceramides were found to colocalize with TJ complexes and follow the same distribution as ZO-1 and claudin-5. Moreover, MS analysis revealed VLC ceramides in TJ isolates. The presence of these VLC ceramides in BRB TJs suggests that like in skin, they might serve a probarrier function in the retinal microvasculature.

Lipidic nature of TJ was first proposed >30 years ago by Kachar and Reese (51) and further supported by freeze fracture preparations that demonstrate the presence of phospholipids and cholesterol particles in TJ strands (52,53). A model of lipid bridges at TJs has been postulated as a route for the lateral transfer of phospholipids and lipid-protein complexes between neighboring cells (54,55). Our study is the first to demonstrate that ceramides colocalize within TJ proteins, as shown by immunofluorescent staining, electron microscopy, and TJ purification, followed

by MS analysis. Specifically, we demonstrated the presence of VLC ceramides and ω-linked AcylCer species by MS analysis of TJ structures. Until now VLC ceramides were only found in the water permeability barrier of the skin.

The exact conformation of ω-linked acyl-VLC ceramides in the TJ structure is not known; however, these very long, highly saturated lipids may have a role in stabilizing TJ proteins and protecting against degradation. Indeed, overexpression of hELOVL4 in BRECs significantly increased occludin content and prevented the VEGF–induced decrease in occludin. This effect was due to translational or posttranslational regulation because the occludin mRNA level was not increased after ELOVL4 overexpression.

Based on the structure, ω-linked acyl-VLC ceramides could be incorporated in the plasma membranes and aid in organizing junctional domain. The long fatty acid tail of ω-linked AcylCers could potentially allow for traversing the thickness of double layer, bridging the space between TJ proteins of apposing cells, and thereby, regulating barrier function. More detailed structural studies would be required to assign the exact function to these lipids in the TJs. In summary, we have shown that ELOVL4-mediated production of VLC ceramides is necessary for retinal endothelial barrier function. Overexpression of ELOVL4 prevented diabetes-induced retinal permeability and BRB breakdown. VLC ceramides may be necessary for TJ stability and thereby enhancing barrier property. Normalization of retinal ELOVL4 expression may provide a potential therapeutic strategy for the prevention of diabetes-induced early breakdown of the BRB by modulating retinal sphingolipid metabolism.

Acknowledgments. The authors acknowledge the technical support provided by Amy S. Porter and Kathleen A. Joseph at the Michigan State University Investigative HistoPathology Laboratory research facility, and Alicia Withrow from Michigan State University Center for Advanced Microscopy. MS analysis was provided by the Molecular Metabolism & Disease Collaborative Mass Spectrometry Core at Michigan State University.

Funding. The research was supported by JDRF Fellowship 3-PDF-2014-108-A-N to Q.W.; National Institutes of Health (NIH) National Eye Institute grants EY-016077 and EY-025383 to J.V.B. and EY-012021 to D.A.A.; funds from core NIH grants P30-EY-007003 and National Institute of Diabetes and Digestive and Kidney Diseases DK-020572; the Jules and Doris Stein Professorship to D.A.A.; and Michigan AgBioResearch grant MICL02163 to J.V.B.

Funding sources had no role in study design, data collection, data analysis, interpretation, writing of the manuscript, or the decision to submit the manuscript for publication.

Duality of Interest. No potential conflicts of interest relevant to this article were reported.

Author Contributions. N.M.K., X.L., T.A.L., M.H.S., S.N., Q.W., S.S.H., S.O., and C.H. performed research. N.M.K., X.L., D.A.A., and J.V.B. designed research. N.M.K., D.A.A., and J.V.B. wrote the manuscript. S.S.S., A.A., V.A.C., S.L.B., and W.W.H. designed, tested, and produced viral vectors. D.A.A. and J.V.B. are the guarantors of this work and, as such, had full access to all the data in the study and take responsibility for the integrity of the data and the accuracy of the data analysis.

References

1. Antonetti DA, Barber AJ, Hollinger LA, Wolpert EB, Gardner TW. Vascular endothelial growth factor induces rapid phosphorylation of tight junction proteins occludin and zonula occluden 1. A potential mechanism for vascular permeability in diabetic retinopathy and tumors. J Biol Chem 1999;274:23463–23467

2. Murakami T, Felinski EA, Antonetti DA. Occludin phosphorylation and ubiquitination regulate tight junction trafficking and vascular endothelial growth factor-induced permeability. J Biol Chem 2009;284:21036–21046

3. Harhaj NS, Felinski EA, Wolpert EB, Sundstrom JM, Gardner TW, Antonetti DA. VEGF activation of protein kinase C stimulates occludin phosphorylation and contributes to endothelial permeability. Invest Ophthalmol Vis Sci 2006;47:5106–5115

4. Zhu W, London NR, Gibson CC, et al. Interleukin receptor activates a MYD88-ARNO-ARF6 cascade to disrupt vascular stability. Nature 2012;492:252–255

5. Aveleira CA, Lin CM, Abcouwer SF, Ambrósio AF, Antonetti DA. TNF-α signals through PKCζ/NF-κB to alter the tight junction complex and increase retinal endothelial cell permeability. Diabetes 2010;59:2872–2882

6. Behzadian MA, Wang X, Windsor LJ, Ghaly N, Caldwell RB. TGF-beta increases retinal endothelial cell permeability by increasing MMP-9: possible role of glial cells in endothelial barrier function. Invest Ophthalmol Vis Sci 2001;42:853–859

7. Kim J, Kim C-S, Lee YM, Jo K, Shin SD, Kim JS. Methylglyoxal induces hyperpermeability of the blood-retinal barrier via the loss of tight junction proteins and the activation of matrix metalloproteinases. Graefes Arch Clin Exp Ophthalmol 2012;250:691–697

8. Enge M, Bjarnegård M, Gerhardt H, et al. Endothelium-specific platelet-derived growth factor-B ablation mimics diabetic retinopathy. EMBO J 2002;21:4307–4316

9. Gavard J, Patel V, Gutkind JS. Angiopoietin-1 prevents VEGF-induced endothelial permeability by sequestering Src through mDia. Dev Cell 2008;14:25–36

10. Cunha-Vaz J, Ribeiro L, Lobo C. Phenotypes and biomarkers of diabetic retinopathy. Prog Retin Eye Res 2014;41:90–111

11. Engerman RL, Kern TS. Experimental galactosemia produces diabetic-like retinopathy. Diabetes 1984;33:97–100

12. Antonetti DA, Barber AJ, Khin S, Lieth E, Tarbell JM, Gardner TW; Penn State Retina Research Group. Vascular permeability in experimental diabetes is associated with reduced endothelial occludin content: vascular endothelial growth factor decreases occludin in retinal endothelial cells. Diabetes 1998;47:1953–1959

13. Giacco F, Brownlee M. Oxidative stress and diabetic complications. Circ Res 2010;107:1058–1070

14. Chew EY, Ambrosius WT, Davis MD, et al.; ACCORD Study Group; ACCORD Eye Study Group. Effects of medical therapies on retinopathy progression in type 2 diabetes. N Engl J Med 2010;363:233–244

15. Tikhonenko M, Lydic TA, Wang Y, et al. Remodeling of retinal fatty acids in an animal model of diabetes: a decrease in long-chain polyunsaturated fatty acids is associated with a decrease in fatty acid elongases Elovl2 and Elovl4. Diabetes 2010;59:219–227

16. Opreanu M, Tikhonenko M, Bozack S, et al. The unconventional role of acid sphingomyelinase in regulation of retinal microangiopathy in diabetic human and animal models. Diabetes 2011;60:2370–2378

17. Opreanu M, Lydic TA, Reid GE, McSorley KM, Esselman WJ, Busik JV. Inhibition of cytokine signaling in human retinal endothelial cells through downregulation of sphingomyelinases by docosahexaenoic acid. Invest Ophthalmol Vis Sci 2010;51:3253–3263

18. Uchida Y. The role of fatty acid elongation in epidermal structure and function. Dermatoendocrinol 2011;3:65–69

19. Kihara A. Very long-chain fatty acids: elongation, physiology and related disorders. J Biochem 2012;152:387–395

20. Mandal MN, Ambasudhan R, Wong PW, Gage PJ, Sieving PA, Ayyagari R. Characterization of mouse orthologue of ELOVL4: genomic organization and spatial and temporal expression. Genomics 2004;83:626–635

21. Agbaga MP, Mandal MN, Anderson RE. Retinal very long-chain PUFAs: new insights from studies on ELOVL4 protein. J Lipid Res 2010;51:1624–1642

22. Agbaga MP, Brush RS, Mandal MNA, Henry K, Elliott MH, Anderson RE. Role of Stargardt-3 macular dystrophy protein (ELOVL4) in the biosynthesis of very long chain fatty acids. Proc Natl Acad Sci U S A 2008;105:12843–12848

23. Busik JV, Esselman WJ, Reid GE. Examining the role of lipid mediators in diabetic retinopathy. Clin Lipidol 2012;7:661–675

24. Wertz PW, Downing DT. Ceramides of pig epidermis: structure determination. J Lipid Res 1983;24:759–765
25. Imokawa G, Abe A, Jin K, Higaki Y, Kawashima M, Hidano A. Decreased level of ceramides in stratum corneum of atopic dermatitis: an etiologic factor in atopic dry skin? J Invest Dermatol 1991;96:523–526
26. Vasireddy V, Uchida Y, Salem N Jr., et al. Loss of functional ELOVL4 depletes very long-chain fatty acids (> or =C28) and the unique ω-O-acylceramides in skin leading to neonatal death. Hum Mol Genet 2007;16:471–482
27. McMahon A, Butovich IA, Mata NL, et al. Retinal pathology and skin barrier defect in mice carrying a Stargardt disease-3 mutation in elongase of very long chain fatty acids-4. Mol Vis 2007;13:258–272
28. Li W, Sandhoff R, Kono M, et al. Depletion of ceramides with very long chain fatty acids causes defective skin permeability barrier function, and neonatal lethality in ELOVL4 deficient mice. Int J Biol Sci 2007;3:120–128
29. Okuda A, Naganuma T, Ohno Y, et al. Hetero-oligomeric interactions of an ELOVL4 mutant protein: implications in the molecular mechanism of Stargardt-3 macular dystrophy. Mol Vis 2010;16:2438–2445
30. Zhang K, Kniazeva M, Han M, et al. A 5-bp deletion in ELOVL4 is associated with two related forms of autosomal dominant macular dystrophy. Nat Genet 2001; 27:89–93
31. Abcouwer SF, Lin CM, Wolpert EB, et al. Effects of ischemic preconditioning and bevacizumab on apoptosis and vascular permeability following retinal ischemia-reperfusion injury. Invest Ophthalmol Vis Sci 2010;51:5920–5933
32. Ryals RC, Boye SL, Dinculescu A, Hauswirth WW, Boye SE. Quantifying transduction efficiencies of unmodified and tyrosine capsid mutant AAV vectors in vitro using two ocular cell lines. Mol Vis 2011;17:1090–1102
33. Wigglesworth VB. Lipid staining for the electron microscope: a new method. J Cell Sci 1975;19:425–437
34. Mahendrasingam S, Wallam CA, Hackney CM. Two approaches to double post-embedding immunogold labeling of freeze-substituted tissue embedded in low temperature Lowicryl HM20 resin. Brain Res Brain Res Protoc 2003;11:134–141
35. Tang VW. Proteomic and bioinformatic analysis of epithelial tight junction reveals an unexpected cluster of synaptic molecules. Biol Direct 2006;1:37
36. Busik JV, Reid GE, Lydic TA. Global analysis of retina lipids by complementary precursor ion and neutral loss mode tandem mass spectrometry. Methods Mol Biol 2009;579:33–70
37. Lydic TA, Busik JV, Reid GE. A monophasic extraction strategy for the simultaneous lipidome analysis of polar and nonpolar retina lipids. J Lipid Res 2014;55: 1797–1809
38. Byeon SK, Lee JY, Lee J-S, Moon MH. Lipidomic profiling of plasma and urine from patients with Gaucher disease during enzyme replacement therapy by nanoflow liquid chromatography-tandem mass spectrometry. J Chromatogr A 2015;1381: 132–139
39. Wang Q, Navitskaya S, Chakravarthy H, et al. Dual anti-inflammatory and anti-angiogenic action of miR-15a in diabetic retinopathy. EBioMedicine 2016;11:138–150
40. Chakravarthy H, Beli E, Navitskaya S, et al. Imbalances in mobilization and activation of pro-inflammatory and vascular reparative bone marrow-derived cells in diabetic retinopathy. PLoS One 2016;11:e0146829
41. Wang Y, Botolin D, Xu J, et al. Regulation of hepatic fatty acid elongase and desaturase expression in diabetes and obesity [published correction appears in J Lipid Res 2006;47:2353]. J Lipid Res 2006;47:2028–2041
42. Wang Q, Tikhonenko M, Bozack SN, et al. Changes in the daily rhythm of lipid metabolism in the diabetic retina. PLoS One 2014;9:e95028
43. Green CD, Olson LK. Modulation of palmitate-induced endoplasmic reticulum stress and apoptosis in pancreatic β-cells by stearoyl-CoA desaturase and Elovl6. Am J Physiol Endocrinol Metab 2011;300:E640–E649
44. Karan G, Lillo C, Yang Z, et al. Lipofuscin accumulation, abnormal electrophysiology, and photoreceptor degeneration in mutant ELOVL4 transgenic mice: a model for macular degeneration. Proc Natl Acad Sci U S A 2005;102:4164–4169
45. McMahon A, Jackson SN, Woods AS, Kedzierski W. A Stargardt disease-3 mutation in the mouse Elovl4 gene causes retinal deficiency of C32-C36 acyl phosphatidylcholines. FEBS Lett 2007;581:5459–5463
46. Harkewicz R, Du H, Tong Z, et al. Essential role of ELOVL4 protein in very long chain fatty acid synthesis and retinal function. J Biol Chem 2012;287:11469–11480
47. Grayson C, Molday RS. Dominant negative mechanism underlies autosomal dominant Stargardt-like macular dystrophy linked to mutations in ELOVL4. J Biol Chem 2005;280:32521–32530
48. Sommer JR, Estrada JL, Collins EB, et al. Production of ELOVL4 transgenic pigs: a large animal model for Stargardt-like macular degeneration. Br J Ophthalmol 2011; 95:1749–1754
49. Sandhoff R. Very long chain sphingolipids: tissue expression, function and synthesis. FEBS Lett 2010;584:1907–1913
50. McMahon A, Butovich IA, Kedzierski W. Epidermal expression of an Elovl4 transgene rescues neonatal lethality of homozygous Stargardt disease-3 mice. J Lipid Res 2011;52:1128–1138
51. Kachar B, Reese TS. Evidence for the lipidic nature of tight junction strands. Nature 1982;296:464–466
52. Kan FW. Cytochemical evidence for the presence of phospholipids in epithelial tight junction strands. J Histochem Cytochem 1993;41:649–656
53. Feltkamp CA, Van der Waerden AW. Junction formation between cultured normal rat hepatocytes. An ultrastructural study on the presence of cholesterol and the structure of developing tight-junction strands. J Cell Sci 1983;63:271–286
54. Laffafian I, Hallett MB. Lipid-protein cargo transfer: a mode of direct cell-to-cell communication for lipids and their associated proteins. J Cell Physiol 2007;210: 336–342
55. Grebenkämper K, Galla HJ. Translational diffusion measurements of a fluorescent phospholipid between MDCK-I cells support the lipid model of the tight junctions. Chem Phys Lipids 1994;71:133–143